## REVIEW ARTICLE

# Surface magneto-optic Kerr effect

Z. Q. Qiu
*Department of Physics, University of California at Berkeley, Berkeley, California 94720*

S. D. Bader[a)]
*Materials Science Division, Argonne National Laboratory, Argonne, Illinois 60439*

(Received 20 April 1999; accepted for publication 19 November 1999)

The surface magneto-optic Kerr effect (SMOKE) has significantly impacted research on magnetic thin films. This is due to its sensitivity, local probing nature, and experimental simplicity. The polar and longitudinal Kerr effects are characterized by a complex rotation of the plane of polarization of linearly polarized incident light upon reflection from the surface of a ferromagnetic material. The rotation is directly related to the magnetization of the material within the probing region of the light. Light penetrates into metals >20 nm deep, but the SMOKE technique derives its surface sensitivity from the limited thickness of the deposited magnetic film, which can be as thin as one atomic layer. Basic principles, experimental arrangements, and applications of SMOKE are reviewed in order to acquaint the nonspecialist with the technique and place it into perspective. © *2000 American Institute of Physics.* [S0034-6748(00)00103-9]

## I. INTRODUCTION

### A. Discovery of the magneto-optic effect

Today magneto-optic effects are widely applied in magnetic research. However, in the last century magneto-optics[1] was discovered somewhat unexpectedly while physicists were searching for relationships between light and various other forces. Early searches were first conducted to find the interaction of light with electrical fields. It was believed that the effect of electrical fields should be stronger than that of magnetic fields. But in 1825 null results were reported when Sir John Herschel examined the propagation of a beam of polarized light along the axis of a helix carrying an electric current.[2] Even Michael Faraday's original search was focused on the relation between light and electricity. Faraday kept a detailed lab diary, and on August 30, 1845 he recorded his failure to find a change in the polarization of light passing through a liquid that was undergoing electrolysis.[3] It was only when he substituted magnetic for electric forces on Sept. 13 of that year, using an electromagnet with an iron core, that he discovered the magneto-optic effect. He recorded in his lab notebook: ''A piece of heavy glass, which was 2 in. by 1.8 in. and 0.5 of an inch thick, being a silicoborate of lead, was experimented with... when contrary magnetic poles were on the same side there *was an effect produced on the polarized ray*, and thus magnetic force and light were proved to have relations to each other. This fact will most likely prove exceedingly fertile, and of great value in the investigation of conditions of nature force.'' [4] After acquiring a more powerful electromagnet on Sept. 18, he continued the experiment with such zeal that he filled twelve pages of his lab notebook in one day and concluded with the statement: ''An excellent day's work.'' He verified that the effect of the magnet was to rotate the polarization plane of the transmitted light by an angle that depended on the strength of the magnet.

The magneto-optic Kerr effect (MOKE)[5] was discovered by the Rev. John Kerr in 1877 while he was examining the polarization of light *reflected* from a polished electromagnet pole. Kerr ultimately received the Royal Medal in 1898 for research that ranked among the most important subsequent to Faraday's. When he was presented with the Royal Medal, his presenter said it was a wonder that Kerr learned so much with the ''comparatively simple and ineffectual apparatus at his disposal.'' Kerr responded, ''Simple it may be, but not ineffectual; rude, but not crude.'' [6] This statement might represent the nature of this technique as used in the present day adaptations that are the subject of this article, especially when compared to many of the elegant techniques of modern surface science and *nonlinear* optics. But simplicity is a major reason that this technique has in the last decade been so widely embraced to study magnetic thin films.

The application of the magneto-optic Kerr effect to surface magnetism, better known by its acronym the surface magneto-optic Kerr effect (SMOKE), began in 1985. The first experimental system studied was ultrathin Fe films grown epitaxially onto a single crystalline substrate of Au(100).[7] Hysteresis loops for the Fe film with atomic layer sensitivity were successfully obtained as a function of film thickness and temperature. Since then SMOKE has been applied to address various issues in low-dimensional magne-

a)Author to whom correspondence should be addressed; electronic mail: bader@anl.gov

 

tism. Additional interest in SMOKE derives from the recent commercialization of high-density magneto-optic information storage media,[8] and especially by studies of candidate materials for next-generation media based on Co/Pt superlattices.[9] The present work provides a general background to the basic principles and experimental setup of the SMOKE technique, and also highlights contemporary topics in order to provide an appreciation for its value in applications related to basic research on magnetic thin films.

### B. Origin of the magneto-optic effect

Magneto-optics is presently described in the context of either macroscopic dielectric theory or microscopic quantum theory.[10] Macroscopically, magneto-optic effects arise from the antisymmetric, off-diagonal elements in the dielectric tensor. Microscopically, the coupling between the electrical field of the light and the electron spin within a magnetic medium occurs through the spin-orbit interaction. In the following, we give a brief review of the microscopic description of the magneto-optic effect, and leave the detailed macroscopic description to the next section.

As it is well known, the optical properties of a medium are determined by a dielectric tensor that is determined by the motion of the electrons in the medium. Thus, a microscopic description of the magneto-optic effect concerns the different response of the electrons to left- and right-circularly polarized electromagnetic waves. In the proceedings of the Royal Society, Sir William Thomson, in 1856, offered a ''microscopic'' explanation of the Faraday effect by arguing that the particles in the medium under an external magnetic field follow different circular paths, depending on their direction relative to the magnetic field. From a modern viewpoint, this explanation is conceptually correct if we identify Thomson's ''particles'' as being electrons (although the electron had not yet been discovered at that time).

It is worthwhile to first discuss the classical motion of electrons to point out the physical origin of the magneto-optic effect. As a beam of light propagates through a medium, the electrical field of the light generates the motions of the electrons in the medium. Without an external magnetic field, it is obvious that a left-circularly polarized electric field will drive the electrons into left circular motion, and a right-circularly polarized electric field will drive the electrons into left circular motion, and a right-circularly polarized electric field will drive the electrons into right circular motion. The radius of the electron orbit for left and right circular motion will be the same. Since the electric dipole moment is proportional to the radius of the circular orbit, there will be no difference between the dielectric constants for the left- and right-circularly polarized electromagnetic waves. Thus, there will be no Faraday rotation. After an external magnetic field is applied in the propagation direction of the electromagnetic wave, there will be an additional Lorentz force acting on each electron. This force points toward or away from the circle's center for left or right circular motion. Thus, the radius for left circular motion will be reduced and the radius for right circular motion will expand. The difference in the radii of the left- and right-circularly polarized modes will give different dielectric constants correspondingly. Thus, it is the Lorentz force of the external magnetic field that generates the Faraday effect.

Quantum descriptions of the magneto-optic effect have focused on the explanation of the unusual large magneto-optic effect in ferromagnetic materials. Early attempts to explain the much stronger magneto-optic effect in ferromagnetic materials assumed that there exists an effective field, rather than the applied field, that determines the Faraday rotation in ferromagnetic materials. In fact, Voigt found that the effective field is of the order of $10^6-10^7$ Oe to produce the observed Faraday rotation. This magnitude is of the order of the Weiss field that was postulated to account for the existence of ferromagnetism. The nature of the Weiss field remained unexplained until Heisenberg developed the theory that ascribed the origin of magnetism to the exchange interaction among electrons. Although Heisenberg's exchange interaction correctly reveals the origin of magnetism as an effective magnetic field to align the individual spins, this field alone cannot be used to explain the Faraday effect. This is because it is not coupled to the electron motion which determines the dielectric properties of a material. This difficulty was solved in 1932 by Hulme[11] who pointed out that it is the spin-orbit interaction that couples the electron spin to its motion to give rise to the large Faraday rotation in a ferromagnetic. Spin-orbit coupling, $\sim(\nabla V\times\mathbf{p})\cdot\mathbf{s}$, results from the interaction of the electron spin with the magnetic field the electron ''sees'' as it moves through the electric field $-\nabla V$ with momentum $\mathbf{p}$ inside a medium. This interaction couples the magnetic moment of the electron with its motion, thus, connecting the magnetic and optical properties of a ferromagnet. Indeed, to a certain extent, the spin-orbit interaction can be thought of as an effective magnetic field vector potential $\sim s\times\nabla V$ acting on the motion of the electron. For nonmagnetic materials, this effect is not strong, although the spin-orbit interaction is present, because the equal number of spin-up and spin-down electrons cancels the net effect. For ferromagnetic materials, however, the effect manifests itself because of the unbalanced population of electron spins.

Hulme calculated the two refraction indices ($R$ and $L$ polarized) using the Heisenberg model of a ferromagnet, and the Kramers–Heisenberg dispersion formula. This approach represents the refraction index in terms of the eigen energy and matrix elements of the dipole moment operator with respect to the eigenfunctions of the system. Hulme accounted for the difference of the two refraction indices by the energy splitting due to the spin-orbit interaction. He neglected, however, the change of the wave function due to the spin-orbit interaction. This theory is unsatisfying because the quenching of the orbital angular momentum in ferromagnets gives no energy splitting. Kittel showed[12] that it is the change of the wave functions due to the spin-orbit interaction that gives rise to the correct order of magnitude of the difference of the two refraction indices. Argyres[13] later gave a full derivation of the magneto-optic effect in a ferromagnet using perturbation theory. Subsequent works were performed thereafter to calculate the magneto-optic effect in different regimes.[14–16]

## II. MACROSCOPIC FORMALISM FOR MAGNETIC MULTILAYERS

Macroscopic descriptions of the magneto-optic effect are based on an analysis of the dielectric properties of a medium. In analogy with mechanical vibrations of a particle, Maxwell expressed linearly polarized light as being a superposition of two circularly polarized components, and realized that the Faraday effect is a result of the different propagating velocities of the two circular modes.[17] This explanation remains the phenomenological explanation of the Faraday effect given in introductory physics textbooks. Looked at in greater detail, there are actually two processes taking place for light propagating in a magnetized medium. First, the two circularly polarized modes gain different phase shifts due to their different propagating velocities, resulting in a rotation of the polarization plane. This process is the conventional Faraday rotation. Second, the different absorption rates of the medium for the two circularly polarized modes affects the ellipticity. In general, both effects exist in a magnetized medium.

The $3\times3$ dielectric tensor of a medium, $\epsilon_{ij}$ with $i,j=1,2,3$, can be decomposed into a symmetric part and an antisymmetric part, $\epsilon_{ij}=(\epsilon_{ij}+\epsilon_{ji})/2+(\epsilon_{ij}-\epsilon_{ji})/2$. The symmetric part can be diagonalized by an appropriate rotation of the coordinate system, thus it does not give rise to the Faraday effect. Since the symmetric part of $\epsilon_{ij}$ is unimportant to the Faraday effect, we will always assume that it is isotropic with dielectric constant $\epsilon_0$. To see the effect of the antisymmetric part of the dielectric tensor, let us consider the following dielectric tensor:

$$\tilde{\epsilon}=\epsilon\begin{pmatrix}1 & iQ_z & -iQ_y\\ -iQ_z & 1 & iQ_x\\ iQ_y & -iQ_x & 1\end{pmatrix}. \tag{1}$$

The two normal modes are left-circularly polarized light with refraction index $n_L=n(1-\frac{1}{2}\ \mathbf{Q}\cdot\hat{k})$, and right-circularly polarized light with refraction index $n_R=n(1+\frac{1}{2}\ \mathbf{Q}\cdot\hat{k})$, where $n=\sqrt{\epsilon}$ is the average refraction index, $\mathbf{Q}=(Q_x,Q_y,Q_z)$ is called the Voigt[18] vector, and $\hat{\mathbf{k}}$ is the unit vector along the direction of the light propagation. Thus, the complex Faraday rotation of the polarization plane after the light has traveled a distance $L$ through the medium is

$$\theta=\frac{\pi L}{\lambda}(n_L-n_R)=-\frac{\pi L n}{\lambda}\mathbf{Q}\cdot\hat{k}. \tag{2}$$

The real part of Eq. (2) gives the rotation, and the imaginary part gives the ellipticity. It is interesting to ask why an external magnetic field has a stronger effect on the polarization plane of light than an external electrical field. Phenomenologically, this can be answered by a simple argument based on time reversal symmetry. Under the time reversal operation, the displacement **D** and electric field **E** vectors remain unchanged, but the magnetic field $H$ changes sign. Thus, Onsager's relation gives $\epsilon_{ij}(E,H)=\epsilon_{ji}(E,-H)$. By expanding $\epsilon_{ij}$ up to terms linear in $E$ and $H$ it becomes obvious that the antisymmetric part of $\epsilon_{ij}$ is generated by the magnetic field. The magnetic field is only one special case of time-reversal symmetry breaking. In general, any quantity that breaks time reversal symmetry could, in principle, generate antisymmetric elements of the dielectric tensor, and, thus, a Faraday rotation.

Since most magnetic materials of interest are metals that strongly absorb light, it is convenient to experimentally measure the reflected light in order to probe the magneto-optic effect. Therefore, the general macroscopic formalism is for the magneto-optic *Kerr* effect although the formalism can be readily extended to include the Faraday effect. Zak *et al.*[19,20] developed a general expression for the Kerr signal based on this method. We will outline the theoretical structure and results here.

For a given magnetic multilayer the refraction tensor for each layer can be expressed by a $3\times3$ matrix. The goal is to calculate the final reflectivity along different polarization directions. The general method is to apply Maxwell's equations to the multilayer structure, and to satisfy the boundary conditions at each interface. The essential part of the theory is to derive two matrices which relate the electric fields at each interface. The first matrix (A) is the $4\times4$ *medium boundary matrix*. It relates the tangential components of the electric and magnetic fields with the *s* and *p* components of the electric field. The second matrix (D) is the $4\times4$ *medium propagation matrix*. It relates the *s* and *p* components of the electric field at the two surfaces of a film of thickness *d*. With the A and D matrices (see Appendix for details), one can calculate the magneto-optic effect under any conditions.

Consider a multilayer structure that consists of $N$ individual layers, and a beam of light impinging on the top of the structure from initial medium *i*. After multiple reflections, there will be a reflected beam backscattered into medium *i*, and a transmitted beam that emerges from the bottom layer into the final medium *f* (Fig. 1). The electric fields in medium *i* and *f* can be expressed

$$P_i=\begin{pmatrix}E_S^i\\ E_p^i\\ E_S^r\\ E_p^r\end{pmatrix}_i=\begin{pmatrix}E_S^i\\ E_p^i\\ r_{ss}E_S^i+r_{sp}E_p^i\\ r_{ps}E_S^i+r_{pp}E_p^i\end{pmatrix}$$

and

$$P_f=\begin{pmatrix}E_S^i\\ E_p^i\\ 0\\ 0\end{pmatrix}_f=\begin{pmatrix}t_{ss}E_S^i+t_{sp}E_p^i\\ t_{ps}E_S^i+t_{pp}E_p^i\\ 0\\ 0\end{pmatrix}, \tag{3}$$

where $r$ and $t$ are reflection and transmission coefficients of the corresponding components, and superscripts $i$ and $r$ define the incident and reflected waves at each boundary between two layers. If $P_m$ is the field component at the bottom surface in the $m$th layer, then the relation between $P_i$ and $P_f$ can be expressed as

$$\begin{aligned}A_iP_i&=A_1D_1P_1=A_1D_1A_1^{-1}A_1P_1\\ &=A_1D_1A_1^{-1}A_2D_2P_2\\ &=\ldots=\prod_{m=1}^{N}(A_mD_mA_m^{-1})A_fP_f.\end{aligned} \tag{4}$$

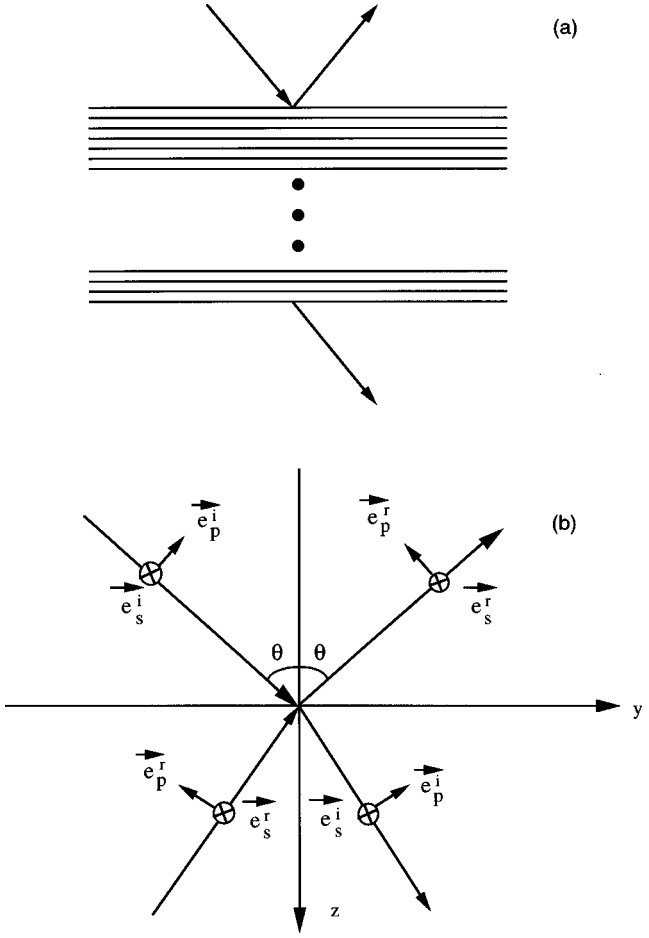


FIG. 1. (a) Schematic of a multilayer structure; (b) definitions of the *s* and *p* directions for the incidence and reflection waves at the boundary between two media.

If this expression is put in the form of $P_i = TP_f$, where

$$T = A_i^{-1} \prod_{m=1}^{N} (A_m D_m A_m^{-1}) A_f \equiv \begin{pmatrix} G & H \\ I & J \end{pmatrix}, \tag{5}$$

then the $2\times 2$ matrices $G$ and $I$ can be used to obtain the Fresnel reflection and transmission coefficients

$$G^{-1} = \begin{pmatrix} t_{ss} t_{sp} \\ t_{ps} t_{pp} \end{pmatrix} \quad \text{and} \quad IG^{-1} = \begin{pmatrix} r_{ss} r_{sp} \\ r_{ps} r_{pp} \end{pmatrix}. \tag{6}$$

The Kerr rotation $\phi'$ and ellipticity $\phi''$ for *s*-and *p*-polarized light are then given by

$$\phi_s = \phi_s' + i\phi_s'' = \frac{r_{ps}}{r_{ss}} \quad \text{and} \quad \phi_p = \phi_p' + i\phi_p'' = \frac{r_{sp}}{r_{pp}}. \tag{7}$$

In the ultrathin limit the magneto-optic expressions simplify further. For ultrathin films the total optical thickness of the film is much less than the wavelength of the light, $\Sigma_i n_i d_i \ll \lambda$. If the initial and final media are nonmagnetic, then the $2\times 2$ matrices of $G$ and $I$ in Eq. (5) yield the following reflection coefficients:

$$r_{ss} = \frac{n_i \cos\theta_i - n_f \cos\theta_f}{n_i \cos\theta_i + n_f \cos\theta_f},$$

$$r_{pp} = \frac{n_f \cos\theta_i - n_i \cos\theta_f}{n_f \cos\theta_i + n_i \cos\theta_f},$$

$$r_{ps} = -\frac{4\pi}{\lambda} \frac{n_i \cos\theta_i}{(n_i \cos\theta_i + n_f \cos\theta_f)(n_f \cos\theta_i + n_i \cos\theta_f)} \times \left( \cos\theta_f \sum_m d_m n_m^2 Q_z^{(m)} - n_f n_i \sin\theta_i \sum_m d_m Q_y^{(m)} \right), \tag{8}$$

$$r_{sp} = -\frac{4\pi}{\lambda} \frac{n_i \cos\theta_i}{(n_i \cos\theta_i + n_f \cos\theta_f)(n_f \cos\theta_i + n_i \cos\theta_f)} \times \left( \cos\theta_f \sum_m d_m n_m^2 Q_z^{(m)} + n_f n_i \sin\theta_i \sum_m d_m Q_y^{(m)} \right).$$

Here $n_i$, $\theta_i$, and $n_f$, $\theta_f$ are the refractive indices and the incident angles of the initial and final media, $z$ is the surface normal direction, and $y$ is in the plane of incidence and in the film plane. Equation (8) provides a basis for an additivity law for multilayers in the ultrathin limit. This law states that the total Kerr signal is simply a summation of the Kerr signals from each magnetic layer, and is independent of the nonmagnetic spacer layers in the multilayer structure. This additivity law is true only in the limit where the total optical thickness of the layered structure is much less than the wavelength of the incident beam. For thick films, it is obvious that the additivity law must break down because the light attenuates and will not penetrate to the deeper layers of the structure. The additivity law provides a focus for examining data in the ultrathin limit. Altered optical constants in the ultrathin limit and interfacial roughness, of course, can also give rise to new behavior that cannot be described within the context of the additivity law.

## III. EXPERIMENTAL SETUP

An experimental SMOKE setup has the advantage of simplicity, especially for ultrahigh vacuum (UHV) *in situ* measurement. There are several ways to build a SMOKE setup. Here we introduce one of the simplest, which we use frequently. Before discussing the instrumental setup, it is necessary to first discuss the working principle of the experimental method. Consider linear *p*-polarized light reflected from a sample surface. If the sample is nonmagnetic, the reflected light is purely *p* polarized. If the sample is ferromagnetic then the reflection beam should consist of an *s* component ($E_s$) in addition to the dominant *p* component ($E_p$), with $E_s/E_p$ being the Kerr rotation. Therefore, measuring this *s* component will be the goal of the experimental setup. Experimentally, the measurement of the *s* component could be realized by placing a linear polarizer in front of the photodetector to eliminate the *p* component. However, this measurement geometry has the following disadvantage. First, since the photodetector measures the light intensity ($\sim |E_s|^2$), the measured quantity is proportional to the square of the magnetization. Second, it is difficult to quantify the absolute value of the Kerr rotation. This disadvantage

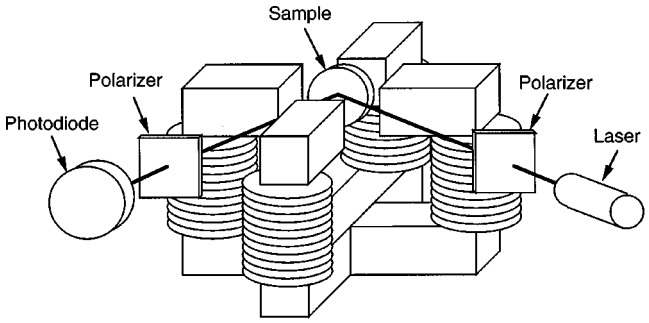


FIG. 2. Schematic drawing of a SMOKE setup.

can be circumvented by setting the polarizer at a small angle ($\delta$) from the $p$ axis. In this way, the intensity measured by the photodetector after the polarizer is

$$I=|E_p \sin\delta+E_s\cos\delta|^2\approx|E_p\delta+E_s|^2. \tag{9}$$

Recall that the expression $E_s/E_p=\phi'+i\phi''$ gives the Kerr rotation $\phi'$ and ellipticity $\phi''$. Then Eq. (9) becomes

$$I=|E_p|^2|\delta+\phi'+i\phi''|^2$$

$$\approx|E_p|^2(\delta^2+2\delta\phi')=I_0\left(1+\frac{2\phi'}{\delta}\right) \tag{10}$$

with

$$I_0=|E_p|^2\delta^2 \tag{11}$$

representing the intensity at zero Kerr rotation. Since both $\phi'$ and $\phi''$ are linearly proportional to the magnetization, the measured intensity as a function of $H$ yields the magnetic hysteresis loop. The saturation Kerr rotation $\phi'_m$ can be determined by the relative change of the Kerr intensity $\Delta I$ obtained upon reversing a field value that is equal to or greater than its saturation value

$$\phi'_m=\frac{\delta}{4}\cdot\frac{\Delta I}{I_0}. \tag{12}$$

In the SMOKE experiment, a laser is usually used as the light source. Typically a low-power (few mW) laser suffices. It is highly desirable to use an intensity-stabilized laser, especially for monolayer studies. Otherwise, the fluctuations of the laser intensity may overwhelm the Kerr signal. The effect of the light intensity drifting during a hysteresis loop measurement (say, of 1–10 s duration) causes a distortion of the hysteresis loop. This effect cannot be eliminated by lock-in techniques. While it is recommended that the SMOKE experiment be performed in a reduced vibration environment an optical table is not necessary, so it is easy to adapt SMOKE to an UHV system. Crystal prism polarizers are useful both for defining the polarization and as an analyzer in front of the photodiode detector. Sheet polarizers can be used, but have a lower extinction ratio when crossed than prism polarizers, and so are not optimal for monolayer studies. Finally, the magnet shown in Fig. 2 consists of two split-coil solenoid pairs. Energizing either pair would generate either a field in the film plane or perpendicular to it for longitudinal or polar measurements, respectively. The dimensions of such a magnet are about 13 cm in height, 15 cm in length, and 4 cm width in the gap. With ~300 turns in the coil, the magnetic field in the gap can reach ~1.5 kOe at a current of 20 A. Wire of 12 or 13 gauge for the coil can carry 10–20 A of current without a heating problem. For *in situ* measurements, the magnet is located inside the vacuum chamber. During the measurement, data are taken as a function of magnetic field to generate an hysteresis loop. Because of possible drift of the laser intensity, it is recommended that the average of many loops be taken.

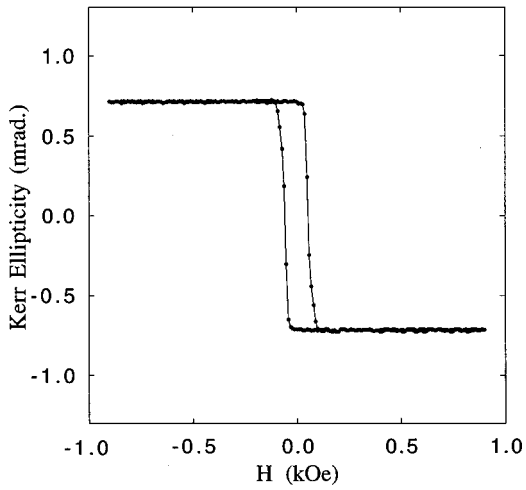


FIG. 3. A SMOKE loop taken from a 6 ML Fe film grown on a Ag(100) substrate.

For *in situ* measurements, the UHV windows used as viewports usually produce a birefringence, $\phi'_w+i\phi''_w$, that prevents the realization of the optical extinction condition. In this situation, a quarter-wave plate is usually placed before the analyzing polarizer to cancel the window birefringence. Then the measured Kerr intensity becomes

$$I=|E_p|^2(\delta^2+2\delta\phi'')=I_0\left(1+\frac{2\phi''}{\delta}\right), \tag{13}$$

i.e., the relative Kerr intensity determines the Kerr ellipticity rather than the rotation in this case. The effect of the quarter-wave plate is to produce a $\pi/2$ phase difference between the $s$ and $p$ components so that the analyzing polarizer will see $i(\phi'+i\phi'')=-\phi''+i\phi'$, i.e., the rotation and ellipticity are interchanged. Then to measure the rotation, a half-wave plate could be used to replace the quarter-wave plate. Then the reflected intensity as a function of the external magnetic field can be used to generate a magnetic hysteresis loop. Figure 3 shows an example of an hysteresis loop measured by SMOKE for a 6 ML Fe/Ag(100) film, where ML denotes monolayer. It quite apparent that SMOKE can readily achieve monolayer sensitivity.

## IV. THE MOKE FAMILY

While the present work is narrowly focused on the SMOKE approach and applications, this section introduces a broader MOKE ''family'' in order to provide a useful perspective and serve as a pointer to the literature. While a number of recent reviews have covered SMOKE,[21–24] historically the primary MOKE spectroscopy involves the determination of wavelength dependent properties.[25] Commer-

cial as well as lab-built spectrometers have been used for such purposes. The main instrumental addition is a white light source and monochrometer. Representative work from the laboratory of Schoenes and co-workers includes basic descriptions of the spectrometers.[26] A recent example involves the giant magneto-optic Kerr rotation observed in single crystals of cerium compounds at low temperatures.[27] In this work a Faraday modulator is used in conjunction with lock-in detection for noise suppression. Faraday modulators have been utilized in other novel configurations,[28] including the quest for anions in high-temperature superconductors.[29]

Lock-in detection techniques have not been discussed with respect to SMOKE because modern computer-controlled experiments can provide the signal averaging needed to improve the signal-to-noise level. In an early SMOKE publication[30] it was even demonstrated that the hysteresis loop collected by means of lock-in detection of the photodiode output and use of an incident beam whose polarization is modulated by a commercial photoelastic modulator was no better than that obtained by the dc method outlined in this review. The place where lock-in techniques and polarization modulation are especially valuable is in the simultaneous magneto-optic characterization of the rotation and ellipticity as a function of wavelength. A recent example of this approach is described in the work of Osgood *et al.*[31] but such work follows the basic outlines provided by pioneers in the field.[32–35] Polarization modulation and related optical techniques are described in a general reference.[36] The influence of imperfections in the polarizer and analyzer were recently analyzed.[37] Polarization modulation has also been used to characterize the Curie temperature of Gd films via *in situ* MOKE studies.[38]

To fill out the range of parameter space and the concomitant phenomena that become physically accessible, a number of variants are now mentioned. New magneto-optic transitions were identified in monolayer-range Fe films using wavelength dependent measurements in the visible region.[39] The measurements were performed *ex situ* and the films were sandwiched between Au layers to protect them from oxidation. Oscillatory effects have been observed in SMOKE signals of wedged structures and attributed to spin-polarized quantum size effects.[40–42] Dynamic scaling of the magnetic hysteresis was studied in the monolayer range for Fe/Au(001),[43] Co/Cu(001),[44] and Fe/W(110)[45] by sweeping the applied magnetic field at rates up to 1 kHz and monitoring the loop area. Magnetic field modulation has been used to obtain ac susceptibilities using an *in situ* MOKE apparatus.[46] Time-resolved MOKE has been extended to the picosecond range. A 30 ps pulsed dye laser was used in a pump-probe experiment in order to study magnetization reversal dynamics in magneto-optic storage materials.[47] Diffraction MOKE is another recent addition due to interest in magnetic nanostructures that consist of arrays of holes[48] or lines (gratings).[49,50] The patterned arrays are of a size and spacing that are comparable to the wavelength of visible light and, thus, they serve as diffraction gratings. The transverse MOKE signals from diffracted beams can be compared to that from the specular beam. Enhanced magneto-optic effects and unique magnetic hysteresis loops are extracted from the signals associated with the diffracted beams. This should continue to provide a wealth of information in the characterization of such nanostructures, as well as challenges in the modeling of the relevant optical and magnetic processes.

A traditional application of MOKE is in magneto-optic imaging of magnetic domain structures. An example is in the characterization of Fe/Cr magnetic multilayers.[51] The technique of differential polarization microscopy was recently introduced that utilizes a Wollaston prism to provide improved image contrast.[52] Wollaston prisms split the signal according to polarization content and can be used quite effectively in all types of MOKE measurements. Transparent magneto-optic indicator films are also used quite effectively to image magnetic domain structures.[53] In this approach a transparent Faraday film is placed on top of the sample of interest. The fringe fields emanating from the sample cause the Faraday-rotation contrast of the indicator film in order to yield the image. This method is sensitive to the perpendicular magnetic response of the sample. However, samples with in-plane magnetization have been imaged in this manner, with the clever addition of drilling holes in the sample, from which perpendicular stray fields emerge. In addition to these types of magneto-optic microscopy, there are ideas under discussion for the extension of such techniques into the near-field region using plasma-resonant Ag particles as probes.[54]

Synchrotron techniques are also popular and of great value in magneto-optic characterizations. A description of synchrotron methods to study magnetic systems has recently become available; the overview stresses the opportunities provided by third-generation synchrotron sources (those for which undulator insertion devices are used to intensify and focus the beam).[55] An advantage is that there is elemental sensitivity since the photon energy can be tuned to exploit the response associated with a specific atomic core level. Synchrotron-based magnetic circular dichroism (MCD) offers selection rules such that the spin and orbital magnetic moments can be separately determined. X-ray MOKE (XMOKE) is rapidly becoming another standard synchrotron technique to characterize magnetic films.

The magneto-optic imaging of antiferromagnetic domain structure has always been a challenging task.[56–58] A recent *tour de force* experiment that combines the use of a third-generation synchrotron source with x-ray magnetic *linear* dichroism spectroscopy and the spatial resolution of a photoelectron emission microscope permitted the imaging of the antiferromagnetic structure at the *surface* of NiO(100).[59] Magnetic linear dichroism of antiferromagnets depends on a second-order effect in the magnetization (as does the transverse Kerr effect in ferromagnets). Second-order magneto-optic effects in anisotropic thin ferromagnetic films and the analysis of asymmetric hysteresis loops was the subject of a recent article that is largely based on the Ph.D. thesis research of Osgood.[60]

Techniques based on nonlinear magneto-optics and second harmonic generation (SHG) and that utilize pump-probe spectroscopies are rapidly becoming valuable tools in the exploration of magnetic surfaces and interfaces. The identifying acronym is SHMOKE. Fortunately an excellent book

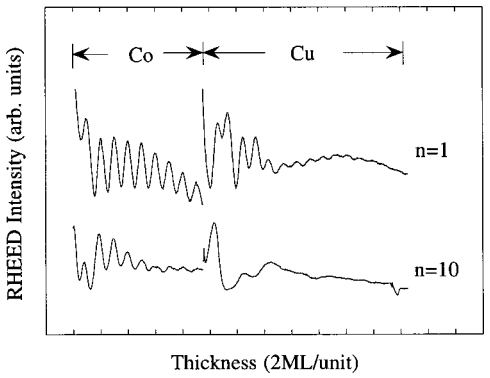


FIG. 4. RHEED oscillations taken during the growth of a $[\mathrm{Co}(9.5\ \mathrm{ML})/\mathrm{Cu}(16\ \mathrm{ML})]_n$ superlattice grown on a Cu(100) substrate.

was recently published that encompasses both experimental and theoretical aspects of the field.[61] Although the signal is weak, so that applications in magnetic recording are not feasible, the enhanced sensitivity to interfaces, and the impressive experimental successes,[62] make this an exciting field to monitor in the future.

Analytical and computational techniques have also undergone a resurgence of activity that has broadened the breadth and scope of MOKE studies. First, there are analyses that are specifically used to motivate new experimental methods for collecting and analyzing data.[63–65] Then there are macroscopic expressions that are useful for simulations,[66–70] and approximations for multilayers based on single-layer equivalences[71] and effective-medium approaches.[72] And finally there are microscopic methods based on first principles to calculate Kerr spectra including surface effects,[73] and for transition metals and multilayers,[74–76] rare earths[77] and actinide systems.[78]

## V. VERIFICATION OF THE MACROSCOPIC FORMULAS

A specific example is now considered for the verification of the macroscopic formulas presented in Sec. II. This work was accomplished by investigating Co overlayers and Co/Cu superlattices.[79] The films were grown epitaxially onto Cu(100) and Cu(111) single-crystal substrates in UHV (base pressure of $2\times10^{-10}$ Torr). The UHV chamber is equipped with reflection high-energy electron diffraction (RHEED), low-energy electron diffraction (LEED), and Auger electron spectroscopy. The Cu substrate single-crystal disks were $\sim1$ cm in diameter, and were mechanically polished down to a $\sim0.25$ $\mu$m paste finish, and then ultrasonically cleaned in methanol before being put into the UHV chamber. Cycles of 3 keV $Ar^+$ sputtering and annealing at 650 °C were used to clean the Cu substrate surfaces *in situ*. After this treatment, well ordered Cu surfaces were formed as indicated by RHEED and LEED. Auger spectroscopy confirmed the cleanliness of the films. The RHEED intensity also was monitored during the growth of the film on the Cu(100) substrate in order to follow the process and to calibrate the thickness monitor. Figure 4 shows the RHEED oscillations during the growth of the Co/Co(100) superlattice. Over 200 RHEED oscillations were observed during the growth. Each oscillation represents the growth of an atomic layer. The persistence of the oscillations indicates a stable, well defined growth mode.

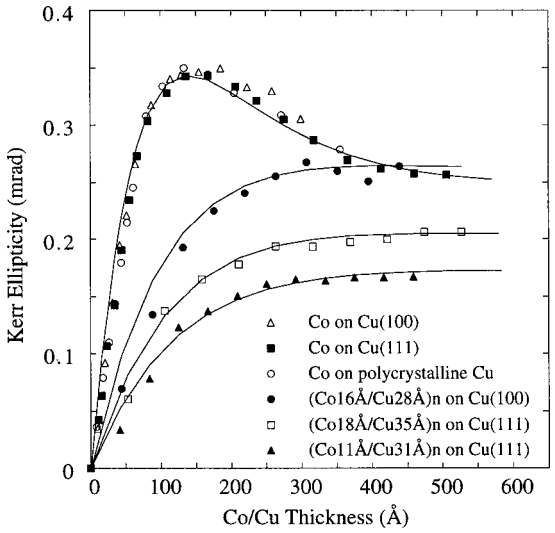


FIG. 5. The Kerr ellipticity measured for different samples. The solid lines are theoretical calculations.

The Kerr ellipticities of the films were measured *in situ* using a He–Ne laser. The angle of incidence was 17°. Results are plotted in Fig. 5. The ellipticity for Co on polycrystal Cu was also measured and shown for comparison. We first concentrate on the magneto-optic behavior of a single Co overlayer on a Cu substrate. The ellipticity data for the overlayers increase linearly in the ultrathin regime, reach a maximum at $\sim$120 Å of Co, and approach a constant value for $>$400 Å of Co. The initial rise is expected since the Kerr effect is sensitive to the increasing amount of Co. In the thick regime, $>$400 Å of Co, the signal saturates since the absorption of light limits the depth sensitivity. In the intermediate regime, the maximum in the ellipticity at $\sim$120 Å of Co is attributed to an optical effect: the reflectivity changes from being dominated by Cu to Co. Since Cu has a higher reflectivity than Co, it acts as a mirror to enhance the signal. Similar behavior was also observed in the Fe/Au system.[80] It is also worth noting that the ellipticity is found to be independent of crystalline orientation in the thickness range studied.

To analyze the data quantitatively, the formalism described in Sec. II was applied to simulate the results. The refractive indices used were obtained from tabulations in the literature:[81] $n_{\mathrm{Cu}}=0.249+3.41i$ and $n_{\mathrm{Co}}=2.25+4.07i$. The values of $Q_1$ and $Q_2$, where $Q=Q_1+iQ_2$, for Co were left as free parameters to best fit the experimental curves; the values $Q_1=0.043$ and $Q_2=0.007$ were obtained. The calculated curves, depicted as the solid lines in Fig. 5, are in good overall agreement with the experimental data. In particular, the peaked behavior of the overlayer data are faithfully reproduced. The ellipticities of three epitaxial Co/Cu superlattices were also measured *in situ* after each Co/Cu bilayer was grown. The superlattices used were $[\mathrm{Co}(16\ \text{Å})/\mathrm{Cu}(28\ \text{Å})]_n$ grown on Cu(100), and $[\mathrm{Co}(11\ \text{Å})/\mathrm{Cu}(31\ \text{Å})]_n$ and $[\mathrm{Co}(18\ \text{Å})/\mathrm{Cu}(35\ \text{Å})]_n$ both grown on Cu(111). The ellipticities of the superlattices appear in Fig. 5 plotted as a func-

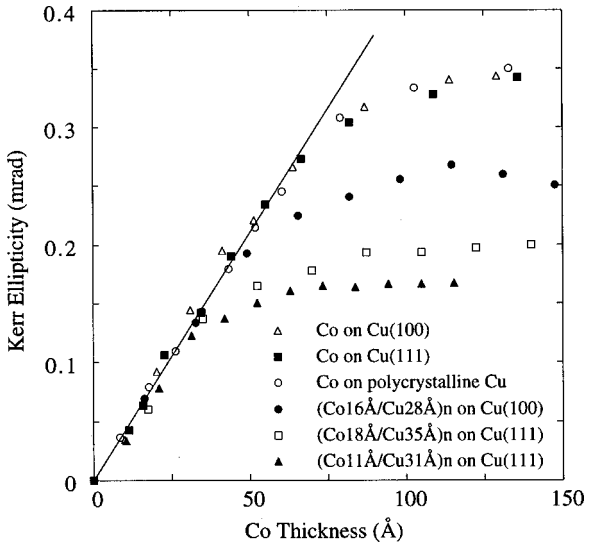


FIG. 6. The additivity law shows that the Kerr signal in the ultrathin regime depends only on the thickness of the magnetic layers.

tion of the total superlattice thickness. Again the ellipticities initially increase linearly in the ultrathin region, and then saturate in thick regime, although there is no maximum at intermediate thickness as for the overlayer cases. The lack of a maximum in the intermediate thickness regime is because the reflectivity is not evolving from that of Cu to that of Co, as in the overlayer cases. Instead, the reflectivity maintains itself at an average value between the two limits, since both Co and Cu remain within the penetration depth of the light, no matter how thick the superlattice becomes. Using the $Q$ value obtained from the Co overlayers, the Kerr ellipticities for the superlattices were calculated and plotted in Fig. 5. The agreement with the experimental data is obvious.

To test the additivity law, the experimental data from Fig. 5 were replotted in Fig. 6 as a function of the thickness of only the magnetic Co layers, as opposed to the total superlattice thickness. All the data in the ultrathin regime then fall onto a single straight line. This result confirms the additivity law that the total Kerr signal in the ultrathin regime is a summation of the Kerr signal from each individual *magnetic* layer and is independent of the thickness of the nonmagnetic spacer layers.

## VI. APPLICATIONS OF SMOKE IN TWO-DIMENSIONAL MAGNETIC THIN FILMS

In addition to the simplicity of the SMOKE setup as an *in situ* magnetic measurement technique, the two great advantages of the SMOKE are its high sensitivity and local probe nature. These two characteristics make SMOKE a popular choice to address issues in thin film magnetism. Two examples are included below to highlight the application of SMOKE.

### A. Spin-reorientation transition

The investigation of the two-dimensional (2D) spin-reorientation transition (SRT) was originally motivated as a test of the Mermin–Wagner theorem.[82] This theorem addresses the most fundamental issue in thin film magnetism—the existence of magnetic long-range order (LRO) in 2D. Mermin and Wagner proved that quantum fluctuations in a 2D isotropic Heisenberg lattice destroys the LRO at finite temperature. Experimentally, however, the Curie temperature ($T_C$) in most 2D magnetic films is finite. This seeming contradiction suggests that, in addition to the Heisenberg exchange interaction, there must exist other energy terms in magnetic thin films. Such energy terms are referred to as the magnetic anisotropies; these terms favor electron spin orientations in particular directions. In a lattice with cubic symmetry (fcc and bcc, for example), it can be shown that the lowest-order term in the anisotropy energy is quartic in the magnetization $M$. However, when translational symmetry along one direction is broken, a larger, square-term anisotropy can be generated along the surface normal direction. This term is often referred to as the magnetic surface anisotropy. A discussion of the origin of the magnetic anisotropy is provided in the next section. Nevertheless, a real magnetic thin film should be better described by an isotropic Heisenberg exchange, a magnetic surface anisotropy ($K_S$), and a shape anisotropy ($-2\pi M^2$) which originates from the short-range part of the dipole–dipole interaction. The direction of the easy axis of magnetization is determined by the sign of the *effective* surface anisotropy $K_{\text{eff}}=K_S/d-2\pi M^2$, where $d$ is the film thickness. For systems with $K_S>0$, a magnetization perpendicular to the film plane can be stabilized at low temperature and below certain thicknesses. Changing temperature or thickness can cause $K_{\text{eff}}$ to vanish at some point below $T_C$, and for the film to approach more closely the ideal realization of an isotropic 2D Heisenberg system. At $K_{\text{eff}}=0$ the spin-reorientation transition should occur wherein $M$ changes its direction from perpendicular to in plane. The question of interest regards the presence or absence of LRO at the transition. Early theoretical studies[83] suggested that in the vicinity of the SRT, there is a region in temperature $\Delta T_R$ wherein the magnetic LRO is lost.

Several groups have carried out experiments on this subject. The first experiments were reported by Pappas Kämper, and Hopster[84] using spin-polarized electron spectroscopy to characterize the systems Fe/Cu(100) and Fe/Ag(100). They found that at low temperature the easy axis was normal to the surface plane, at high temperature it was in plane, and in the SRT region there was a temperature gap ~20 K wide within which the magnetic remanence vanished. Then the Fe/Ag(100) system was studied via SMOKE as a function of both temperature and film thickness. It was found that the magnetization is not identically zero in the transition region, but is markedly reduced and exhibits structure in a ''pseudo gap'' that resembles an asymmetric ramping toward zero with increasing temperature or film thickness.[85] Thus, the gap, if it exists, must be at least an order of magnitude smaller than the ~20 K reported by Pappas and co-workers.

To illustrate the advantage of the local probe nature of the SMOKE technique, we limit the discussion to address the thickness dependent data only. To explore the detailed features within the SRT region, many samples with different film thicknesses are needed. This is because sample-to-sample variations are known to occur throughout surface science and thin-film growth that cannot be adequately con-

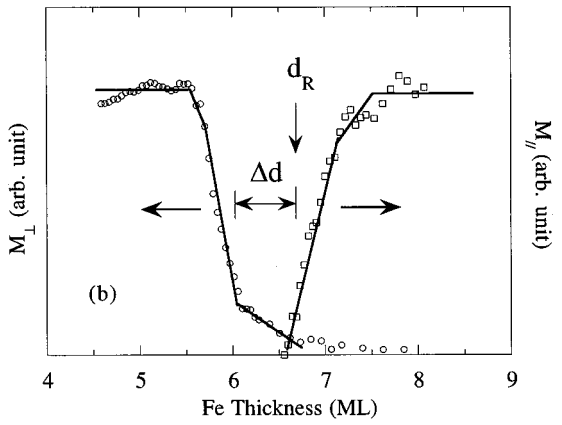


FIG. 7. Spin reorientation transition as a function of film thickness.

trolled. This difficulty can be overcome by the use of wedge-shaped samples. Wedged samples provide an essentially continuous change of film thickness within a single specimen so that, as a local probe scans across the sample, the magnetization can be measured for different thicknesses in a systematic manner. SMOKE measures the magnetization within the confines of the laser spot. When applied to the SRT, its thickness resolution can achieve the 0.04 ML level for a typical wedge with, say, a 2 ML mm slope. Figure 5 illustrates the perpendicular magnetic remanence ($M_\perp$) determined from the polar signal, and the parallel remanence ($M_\parallel$) determined from the longitudinal signal, at room temperature for different Fe film thicknesses. The existence of the SRT is evident as a function of the film thickness. At low thicknesses, $M_\perp$ maintains its saturation value, and at large thicknesses, $M_\parallel$ retains its saturation value. However, in the SRT region ($\Delta d$ in Fig. 7), $M$ is greatly suppressed from its saturation value. This region is similar to that observed by Pappas, Kämper, and Hopster in Fe/Cu(100)[84] and Fe/Ag(100) via polarized electron scattering.[86] But the SMOKE measurements definitively show that $M$ is *not zero* in this region. Thus, this region is *not* associated with a loss of LRO, but instead with a *pseudo gap* that suggests the presence of complex magnetic structure.

The formation of magnetic domains within the pseudogap region provides a possible explanation for the suppression of $M$ but without a loss of magnetic LRO. Yafet and Gyorgy were first to recognize that a stripe domain structure has a lower energy than a single domain structure in a 2D system with perpendicular, uniaxial anisotropy.[87] It was found that the domain size increases almost exponentially as the effective surface anisotropy departs from zero. Therefore, the stripe domains are observable only in the vicinity of the SRT where the effective surface anisotropy is nearly zero and the domain size is less than the sample size. This explains why there is a gapped region in the SRT within which the magnetic remanence is greatly suppressed. Stripe domains form a one-dimensional (1D) ordered state which itself is unstable against thermal fluctuations. Indeed, Kashuba and Pokrovsky[88] found that the stripe domain structure is equivalent to a 2D liquid crystal system in that it possesses orientational order but no spatial order. An experimental observation of the stripe domains in the SRT region was presented by Allenspach and Bischof who applied the SEMPA technique to study the SRT in the Fe/Cu(100) system.[89] (SEMPA is a highly surface-sensitive magnetic imaging technique that stands for ''scanning electron microscopy with polarization analysis.'') They observed that the single domain structure of the film breaks into stripe domains ($\sim$1 $\mu$m size) in the gap region. Results of dynamic properties of the SRT are also consistent with a stripe domain structure.[90]

### B. Magnetic anisotropy and lattice symmetry breaking

The Heisenberg exchange interaction is invariant under spatial rotation. In a real lattice, however, the electrons that contribute to the magnetization usually obey the lattice symmetry in their wave functions due to the crystal fields. Thus, the spin-orbit interaction can transfer the lattice symmetry from the electron wave functions to the electron spins to break the spin isotropy. Thus, energy terms exist that favor special directions for the electron spins. This energy is called the magnetocrystalline anisotropy. Given that it originates from the spin-orbit interaction,[91] the magnetic anisotropy must obey the symmetry of the lattice. Understanding how lattice symmetry breaking induces magnetic anisotropy is of fundamental importance.

To isolate the lattice symmetry effect from the electronic effect, a few groups have performed experiments on magnetic thin films grown on stepped (001) substrates.[92–94] The idea is that the atomic steps on the (001) surface break the fourfold rotational symmetry to induce a uniaxial magnetic anisotropy in the film plane. Experimentally, stepped surfaces consist of low Miller-index terraces uniformly separated by atomic steps, and are created by polishing a sample surface that is misaligned by a few degrees from the terrace normal direction. Such surfaces are also referred to as *vicinal* surfaces, because crystallographically they are oriented in the vicinity of fundamental, low Miller-index faces. To experimentally explore the relationship between induced magnetic anisotropy and lattice symmetry breaking, many substrates with different vicinal angles would be needed. In practice, it is difficult to prepare multiple surfaces under identical conditions. To overcome this difficulty, ''curved'' substrates have been introduced to provide a continuous gradation in the step density. Substrates of (001) orientation and 1 cm in diameter are used in the examples we cite below. Half of the surface is polished to retain its [001] orientation and serve as a reference, while the other half is polished with a curvature such that the vicinal angle varies continuously from 0° to 10°. SMOKE has a distinct advantage for this study because the reflection angle of the SMOKE laser beam simultaneously determines the local vicinal angle so that the relation between the step-induced magnetic anisotropy and the step density can be systematically explored from a single *curved* sample.

Results for three representative systems are discussed: Fe/W(001), Co/Cu(001), and Fe/Pd(001). In Fe/W and Fe/Pd, the steps are parallel to the [100] direction of the Fe. For the Co/Cu system, the steps are parallel to the $[1\bar{1}0]$ direction of the Co. The magnetization is in the film plane for all

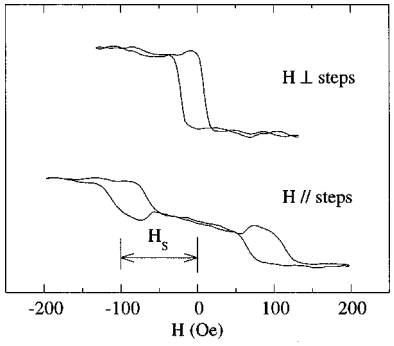


FIG. 8. Hysteresis loops for a 2 ML Fe film grown on a stepped W(001) surface miscut by 4.7°. The square loop is for $H$ perpendicular to the step edges, and the split loop is for $H$ parallel to the step edges.

three systems, thus only longitudinal hysteresis loops are reported. Figure 8 shows hysteresis loops for a 2 ML Fe film grown on stepped W(001) with a 4.7° vicinal angle. The stepped Fe film shows a square loop with ~100% remanence for the applied magnetic field oriented *perpendicular* to the step edges, and two split subloops with zero remanence for the field oriented *parallel* to the step edges. This behavior indicates that the atomic steps indeed induce an in-plane, uniaxial magnetic anisotropy with the easy magnetization axis perpendicular to the step edges. The easy axis of the step-induced anisotropy depends on the physical system. While the Fe/W(001)[95] and Fe/Pd(001)[96] systems have their easy axis *perpendicular* to the step edges, the Co/Cu(001)[97] and Fe/Ag(001)[98] systems have their easy axis *parallel* to the step edges. Nevertheless, the splitting field $H_s$, as defined in Fig. 8 for the hard-axis loop, is proportional to the strength of the step-induced anisotropy. Figure 9 shows the relation between $H_s$ and the vicinal angle $\alpha$ (which is proportional to the step density) for the three systems. Fitting $H_s \sim \alpha^n$ (the solid lines in Fig. 9) yields an exponent $n=2$ for the Fe/W system, but $n=1$ for the Co/Cu and Fe/Pd systems.

To understand why there is different dependence of $H_s$ on $\alpha$ for different systems, one has to examine how the symmetry of the lattice at the step edges is broken for bcc and fcc structures. In the Néel pair-bonding model[99] the magnetic anisotropy is generated by nearest-neighbor bonds. For bcc and fcc lattices, there is no uniaxial anisotropy because contributions from all nearest-neighbor bonds cancel out the square-term anisotropy. At the step edges, however, the missing atoms break this cancellation so that uniaxial anisotropy will be manifest.

For a bcc lattice with steps parallel to the [100] direction, the anisotropy due to the missing atoms should have the form $E_a=-(K/L)u_\eta u_\zeta$, where $L$ is the terrace length, **u** is the unit vector of the magnetization **M**, and $\xi$, $\eta$, and $\zeta$ are the [100], [010], and [001] axes, respectively. For fcc lattice with steps parallel to the $[1\bar{1}0]$ direction, the anisotropy due to the missing atoms has the form $E_a=-\frac{K}{L}(2u_\eta^2+3u_\zeta^2+2\sqrt{2}u_\eta u_\zeta)$, where $\xi=[1\bar{1}0]$, $\eta=[110]$, and $\zeta=[001]$. Note that the normal direction ($z$ axis) of the stepped surface makes a small vicinal angle $\alpha$ to the [001] axis (so that $\alpha \approx 1/L$). The crystal $\xi\eta\zeta$ frame of reference has to be transformed from $u_\zeta=u_x$, $u_\eta=u_y\cos\alpha+u_z\sin\alpha$, and $u_\zeta=-u_y\sin\alpha+u_z\cos\alpha$, into to the film $xyz$ frame with the $x$ and $y$ axes in the film plane parallel and perpendicular to the step edges, respectively. The anisotropy (for small $\alpha$) transforms to $E_a=-K(\alpha u_y u_z-\alpha^2 u_y^2+\alpha^2 u_z^2)$ for a bcc lattice, and $E_a=-K(2\alpha u_y^2+3\alpha u_z^2+2\sqrt{2}\alpha u_y u_z)$ for a fcc lattice. Therefore the in-plane, step-induced anisotropy ($u_z=0$) is $E_a=K\alpha^2 u_y^2$ for the bcc case, and $E_a=-2K\alpha u_y^2$ for fcc. This provides an explanation for why Fe/W and Co/Cu exhibit quadratic and linear $\alpha$ dependences, respectively, for their step-induced anisotropies. The most interesting result is the linear dependence in the Fe/Pd system. Fe has a bcc structure but Pd has fcc structure. It was shown that the Pd at the interface of Fe/Pd is ferromagnetic due to the Fe spin polarization.[100,101] Since Pd has a much stronger spin-orbit interaction than Fe, the Pd is expected to dominate the magnetic anisotropy in the Fe/Pd system. We believe that is why

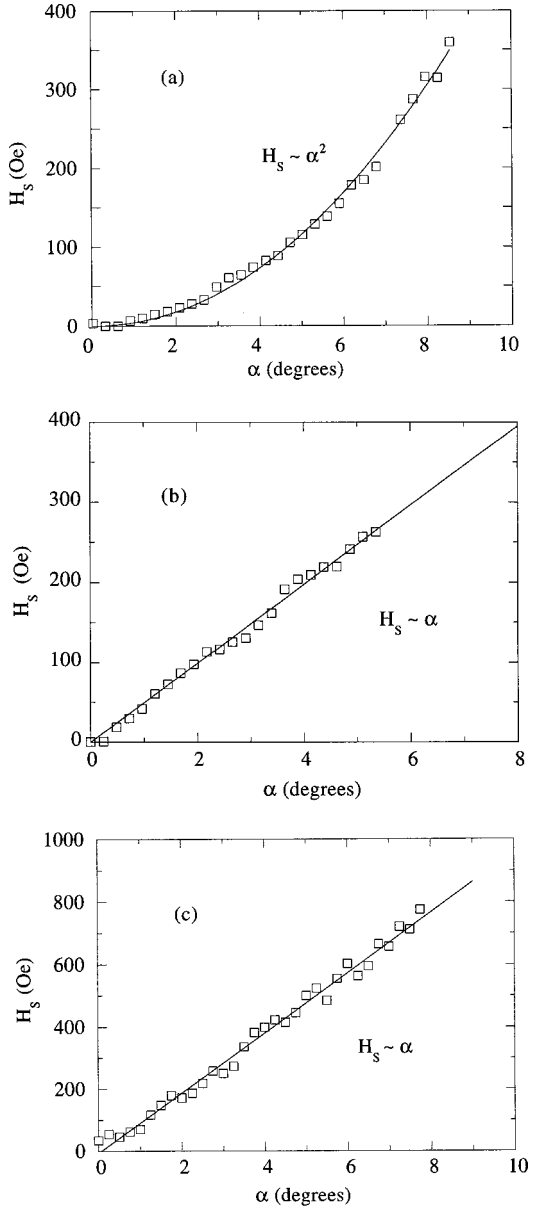


FIG. 9. $H_s$ (from Fig. 8) vs vicinal angle $\alpha$ for (a) Fe/W(001), (b) Co/Cu(001), and (c) Fe/Pd(001). The solid lines are results of a power-law fitting yielding a quadratic relation between $H_s$ and $\alpha$ for the Fe/W system, but a linear relation for the Co/Cu and Fe/Pd systems.

the Fe/stepped Pd(001) system exhibits an $\alpha$-linear dependence of the step-induced anisotropy as for a fcc lattice.

## VII. DISCUSSION

The basic principles, experimental setup, and two applications of the SMOKE technique were outlined. Although SMOKE is a powerful technique, it has certain drawbacks. For example, it cannot distinguish surface or interface magnetism from that arising from the interior layers. This is an area where nonlinear (second harmonic) MOKE (or SHMOKE) has major advantages. SMOKE also cannot, in general, distinguish an antiferromagnetic phase from a nonmagnetic phase. These weaknesses leave many experimental challenges for the future. Also, concerning theoretical challenges, a microscopic understanding of magneto-optics in the monolayer regime is needed since macroscopic continuum theory must ultimately break down. Experimentally, it is also important to enhance both spatial and time resolution so that small scale processes, such as domain wall dynamics, can be investigated. Possible ways to realize this goal involve combining SMOKE with other techniques, such as near-field optical spectroscopy, scanning tunneling microscopy, and/or pump-and-probe methods. In the present article a sense of history as well as of future opportunities was invoked to stimulate interest both in the SMOKE technique and in its impact on modern thin-film and surface magnetism.

## ACKNOWLEDGMENTS

The authors thank the many colleagues that we have worked with on the projects cited in the reference list. Without them this work would not be possible. This work was financially supported by the Office of Basic Energy Sciences-Materials Sciences of the United States Department of Energy under Contract Nos. W-31-109-ENG-38 (at Argonne) and DE-AC03-76SF00098 (at Berkeley) and by National Science Foundation Contract No. DMR-9805222 (at Berkeley).

## APPENDIX

To derive the matrices A and D, it is important to first describe the normal modes of the electromagnetic waves in a magnetic medium. To obtain them, consider a wave $\sim e^{i\mathbf{k}\cdot\mathbf{x}-i\omega t}$ propagating in a medium whose dielectric tensor is described by Eq. (1). Since the magnetic response of the medium is attributed to the Voigt vector $\mathbf{Q}$ in the dielectric tensor, we can assume that the magnetic permeability is 1. Then the relationship between $\mathbf{D}$ and $\mathbf{E}$, and $\mathbf{B}$ and $\mathbf{H}$ is

$$\mathbf{D}=\varepsilon\mathbf{E}+i\varepsilon\mathbf{E}\times\mathbf{Q} \quad \text{and} \quad \mathbf{B}=\mathbf{H}. \tag{A1}$$

Then Maxwell's equations give

$$\begin{cases} \mathbf{k}\cdot\mathbf{E}+i\mathbf{k}\cdot(\mathbf{E}\times\mathbf{Q})=0 \\ \mathbf{k}\times\mathbf{E}=\dfrac{\omega}{c}\mathbf{H} \\ \mathbf{k}\cdot\mathbf{H}=0 \\ \mathbf{k}\times\mathbf{H}=-\dfrac{\omega\varepsilon}{c}(\mathbf{E}+i\mathbf{E}\times\mathbf{Q}) \end{cases}. \tag{A2}$$

It is easy to see that $\mathbf{D}$, $\mathbf{B}$ (or $\mathbf{H}$) and $\mathbf{k}$ are perpendicular to each other. The $\mathbf{E}$ vector, however, has a component parallel to the wave vector $\mathbf{k}$. Using the familiar *s*- and *p*- polarization modes, the electric field can be written as

$$\mathbf{E}=E_s\mathbf{e}_s+E_p\mathbf{e}_p+i(-\mathbf{Q}\cdot\mathbf{e}_pE_s+\mathbf{Q}\cdot\mathbf{e}_sE_p)\mathbf{e}_k\,. \tag{A3}$$

Here $\mathbf{e}_s$, $\mathbf{e}_p$, and $\mathbf{e}_k$ are unit vectors along the *s*, *p*, and *k* directions. $E_s$ and $E_p$ are the *s* and *p* components of the electric field, and their equations of motion are

$$\begin{cases} \left(\dfrac{\omega^2\varepsilon}{c^2}-k^2\right)E_s+\dfrac{i\omega^2\varepsilon\mathbf{Q}\cdot\mathbf{e}_k}{c^2}E_p=0 \\ -\dfrac{i\omega^2\varepsilon\mathbf{Q}\cdot\mathbf{e}_k}{c^2}E_s+\left(\dfrac{\omega^2\varepsilon}{c^2}-k^2\right)E_p=0 \end{cases}. \tag{A4}$$

To first order in $Q$, it is easy to show that the two normal modes are right ($R$)- and left ($L$)-circularly polarized modes with

$$k_{R,L}=k(1\pm\tfrac{1}{2}\mathbf{Q}\cdot\mathbf{e}_k) \quad \text{or} \quad n_{R,L}=n(1\pm\tfrac{1}{2}\mathbf{Q}\cdot\mathbf{e}_k). \tag{A5}$$

Here $k=\frac{\omega}{c}\sqrt{\varepsilon}$ and $n=\sqrt{\varepsilon}$ are the wave vector and refraction index, respectively, without the magnetization. After obtaining the two normal modes, any mode of the electromagnetic wave can be viewed as their superposition.

Now, we consider an electromagnetic wave propagating inside a magnetic multilayer structure. At each boundary between two layers, the boundary conditions involve $E_x$, $E_y$, $H_x$ and $H_y$, where *x* and *y* axis are in the film plane and perpendicular and parallel to the incident plane, respectively. It is more convenient to express these four quantities with the *s* and *p* components of the electric field. The *x* components are easy to write because they are parallel to the *s* direction

$$E_x=E_s^i+E_s^r, \tag{A6}$$

where the superscripts *i* and *r* denote the incident and reflected waves, respectively. For the *y* components, one has to keep in mind that the electric field has a component $i(-\mathbf{Q}\cdot\mathbf{e}_pE_s+\mathbf{Q}\cdot\mathbf{e}_sE_p)\mathbf{e}_k$ parallel to the $\mathbf{k}$ direction, and that the $L$ and $R$ modes have different refraction indices and incident angles. Then $E_y$ can be expressed as

$$\begin{aligned} E_y=&E_p^{i,L}\cos\theta_L+E_p^{i,R}\cos\theta_R+i(-\mathbf{Q}\cdot\mathbf{e}_p^iE_s^i+\mathbf{Q}\cdot\mathbf{e}_s^i\mathbf{E}_p^i) \\ &\times\sin\theta-E_p^{r,L}\cos\theta_L-E_p^{r,R}\cos\theta_R \\ &+i(-\mathbf{Q}\cdot\mathbf{e}_p^rE_s^r+\mathbf{Q}\cdot\mathbf{e}_s^rE_p^r)\sin\theta. \end{aligned} \tag{A7}$$

Using the relations

$$\begin{cases} E_p^L=+iE_s^L \\ E_p^R=-iE_s^R \\ n_R\sin\theta_R=n_L\sin\theta_L=n\sin\theta \end{cases}, \tag{A8}$$

$E_y$ can be expressed as

$$E_y=\frac{i}{2}[-Q_y\tan\theta(1+\cos^2\theta)+Q_z\sin^2\theta]E_s^i + (\cos\theta+iQ_x\sin\theta)E_p^i+\frac{i}{2}[Q_y\tan\theta(1+\cos^2\theta) + Q_z\sin^2\theta]E_s^r+(-\cos\theta+iQ_x\sin\theta)E_p^r. \quad \text{(A9)}$$

$H_x$ and $H_y$ can be derived in a similar way from the expression $\mathbf{k}\times\mathbf{E}=\omega/c\mathbf{H}$:

$$H_x=\frac{in}{2}(Q_y\sin\theta+Q_z\cos\theta)E_s^i-nE_p^i + \frac{in}{2}(Q_y\sin\theta-Q_z\cos\theta)E_s^r-nE_p^r,$$

$$H_y=n\cos\theta E_s^i+\frac{in}{2}(Q_y\tan\theta+Q_z)E_p^i - n\cos\theta E_s^r-\frac{in}{2}(Q_y\tan\theta-Q_z)E_p^r. \quad \text{(A10)}$$

Therefore, we obtain the relation between the $x$ and $y$ components of $\mathbf{E}$ and $\mathbf{H}$ with $s$ and $p$ components of the electric field. This relation can be expressed as a matrix product

$$\begin{pmatrix} E_x \\ E_y \\ H_x \\ H_y \end{pmatrix} = A \begin{pmatrix} E_s^i \\ E_p^i \\ E_s^r \\ E_p^r \end{pmatrix} \quad \text{(A11)}$$

with the $4\times4$ matrix A known as the *medium boundary matrix*

$$A=\begin{pmatrix} 1 & 0 & 1 & 0 \\ \frac{i}{2}[-Q_y\tan\theta(1+\cos^2\theta)+Q_z\sin^2\theta] & \cos\theta+iQ_x\sin\theta & \frac{i}{2}[Q_y\tan\theta(1+\cos^2\theta)+Q_z\sin^2\theta] & -\cos\theta+iQ_x\sin\theta \\ \frac{in}{2}(Q_y\sin\theta+Q_z\cos\theta) & -n & \frac{in}{2}(Q_y\sin\theta-Q_z\cos\theta) & -n \\ n\cos\theta & \frac{in}{2}(Q_y\tan\theta+Q_z) & -n\cos\theta & -\frac{in}{2}(Q_y\tan\theta-Q_z) \end{pmatrix}. \quad \text{(A12)}$$

The next step is to derive the propagation matrix which relates $\mathbf{E}$ and $\mathbf{H}$ at the two surfaces of a film of thickness $d$. Since each incident and reflected beam is composed of $L$- and $R$-circularly polarized modes, we use 1 and 2 to denote the $L$ and $R$ modes of the incident beam at both surfaces, and 3 and 4 to denote the $L$ and $R$ modes of the reflected beam at both surfaces. Then we have the following relations:

$$\begin{cases} E_A^{1,2}=E_B^{1,2}\exp(ik^{1,2}d\cos\theta_{1,2}) \\ E_A^{3,4}=E_B^{3,4}\exp(-ik^{3,4}d\cos\theta_{3,4}). \end{cases} \quad \text{(A13)}$$

The relation between $E_s$ and $E_p$ at boundaries A and B can then be expressed by a matrix product

$$\begin{pmatrix} E_s^i \\ E_p^i \\ E_s^r \\ E_p^r \end{pmatrix}_A = D \begin{pmatrix} E_s^i \\ E_p^i \\ E_s^r \\ E_p^r \end{pmatrix}_B, \quad \text{(A14)}$$

where $D$ is $4\times4$ matrix known as the *medium propagation matrix*.

$$D=\begin{pmatrix} U\cos\delta_i & U\sin\delta_i & 0 & 0 \\ -U\sin\delta_i & U\cos\delta_i & 0 & 0 \\ 0 & 0 & U^{-1}\cos\delta_r & -U^{-1}\sin\delta_r \\ 0 & 0 & U^{-1}\sin\delta_r & U^{-1}\cos\delta_r \end{pmatrix} \quad \text{(A15)}$$

with

$$\begin{cases} U=\exp(-ikd\cos\theta) \\ \delta_i=\frac{kd}{2}(Q_y\tan\theta+Q_z) \\ \delta_r=\frac{kd}{2}(Q_y\tan\theta-Q_z) \end{cases}. \quad \text{(A16)}$$


[1] M. Faraday, Trans. R. Soc. (London) **5**, 592 (1846).
[2] *The Effects of a Magnetic Field on Radiation—Memoirs by Faraday, Kerr and Zeeman*, edited by E. P. Lewis (American, New York, 1990), preface, p. v.
[3] M. Faraday, Diary, 30 August 1845, Vol. 4, pp. 7434, and 7437–7444.
[4] M. Faraday, Diary, 13 September 1845, Vol. 4, p. 7504.
[5] J. Kerr, Philos. Mag. **3**, 339 (1877); **5**, 161 (1878).
[6] See, *Molecular Electro-Optics, Part I, Theory and Methods*, edited by C. T. O'Konski (Dekker, New York, 1976), p. 517.
[7] E. R. Moog and S. D. Bader, Superlattices Microstruct. **1**, 543 (1985); S. D. Bader, E. R. Moog, and P. Grünberg, J. Magn. Magn. Mater. **53**, L295 (1986).
[8] S. Klahn, P. Hansen, and F. J. A. M. Greidanus, Vacuum **41**, 1160 (1990).
[9] K. Nakamura, S. Tsunashima, S. Iwata, and S. Uchiyama, IEEE Trans. Magn. **25**, 3758 (1989); S. Hashimoto, H. Matouda, and Y. Ochiai, Appl. Phys. Lett. **56**, 1069 (1990); S. Hashimoto, Y. Ochiai, and K. Aso, J. Appl. Phys. **67**, 2136 (1990).
[10] L. D. Landau and E. M. Lifshtz, *Electrodynamics of Continuous Media* (Pergamon, London, 1960).
[11] H. R. Hulme, Proc. R. Soc. London, Ser. A **135**, 237 (1932).
[12] C. Kittel, Phys. Rev. **83**, 208(A) (1951).
[13] P. N. Argyres, Phys. Rev. **97**, 334 (1955).
[14] H. S. Bennett and E. A. Stern, Phys. Rev. **137**, A448 (1965).
[15] Y. R. Shen, Phys. Rev. **133**, A51 (1964).
[16] J. E. Erskine and E. A. Stern, Phys. Rev. B **8**, 1239 (1973).

[17] J. C. Maxwell, *Electricity and Magnetism* (1873), Vol. 2, Chap. 21.
[18] W. Voigt, *Magneto- und Elektro-optic* (Teuner, Leipzig, 1908); *Handbook der Elektrizität und des Magnetismus* (Barth, Leipzig, 1915), Vol. IV. 2, p. 39.
[19] J. Zak, E. R. Moog, C. Liu, and S. D. Bader, J. Magn. Magn. Mater. **89**, 107 (1990).
[20] J. Zak, E. R. Moog, C. Liu, and S. D. Bader, Phys. Rev. B **43**, 6423 (1991).
[21] S. D. Bader, J. Magn. Magn. Mater. **100**, 440 (1991).
[22] J. L. Erskine and S. D. Bader, in *Ultrathin Magnetic Structures II*, edited by B. Heinrich and J. A. C. Bland (Springer, Berlin, 1994), pp. 297–325.
[23] Z. Q. Qiu and S. D. Bader, in *Nonlinear Optics in Metals*, edited by K. H. Bennemann (Clarendon, Oxford, 1998), pp. 1–41.
[24] Z. Q. Qiu and S. D. Bader, J. Magn. Magn. Mater. **200**, 664 (1999).
[25] G. S. Krinchik and V. A. Artem'ev, Sov. Phys. JETP **26**, 1080 (1968).
[26] J. Schoenes, Phys. Rep. **66**, 187 (1980).
[27] R. Pittini, J. Schoenes, and P. Wachter, Phys. Rev. B **55**, 7524 (1997).
[28] J. F. Dillon, Jr. E. M. Gyorgy, F. Hellman, L. R. Walker, and R. C. Fulton, J. Appl. Phys. **64**, 6098 (1988).
[29] K. B. Lyons, J. Kwo, J. F. Dillon, Jr., G. P. Espinosa, M. McGlashan-Powell, A. P. Ramirez, and L. F. Schneemeyer, Phys. Rev. Lett. **64**, 2949 (1990).
[30] S. D. Bader and E. R. Moog, J. Magn. Soc. Jpn. **11**, Supplement No. S17 (1987).
[31] R. M. Osgood III, K. T. Riggs, A. E. Johnson, J. E. Mattson, C. H. Sowers, and S. D. Bader, Phys. Rev. B **56**, 2627 (1997).
[32] S. N. Jasperson and S. E. Schnatterly, Rev. Sci. Instrum. **40**, 761 (1969); erratum **41**, 152 (1970)
[33] J. Badoz, M. Billardon, J. C. Canit, and M. F. Russel, J. Opt. **8**, 373 (1977).
[34] K. Sato, Jpn. J. Appl. Phys. **20**, 2403 (1981).
[35] P. Q. J. Nederpel and J. W. D. Martens, Rev. Sci. Instrum. **56**, 687 (1985).
[36] D. S. Kliger, J. W. Lewis, and C. E. Randall, *Polarized Light in Optics and Spectroscopy* (Academic, Boston, 1990).
[37] C.-Y. You and S.-C. Shin, Rev. Sci. Instrum. **68**, 3519 (1997).
[38] M. Farle, W. A. Lewis, and K. Baberschke, Appl. Phys. Lett. **62**, 2728 (1993).
[39] Y. Suzuki, T. Katayama, S. Yoshida, K. Tanaka, and K. Sato, Phys. Rev. Lett. **68**, 3355 (1992).
[40] A. Carl and D. Weller, Phys. Rev. Lett. **74**, 190 (1995).
[41] R. Mégy, A. Bounouh, Y. Suzuki, P. Beaunillain, P. Bruno, C. Chappert, B. Lecuyer, and P. Veillet, Phys. Rev. B **51**, 5586 (1995).
[42] Y. Suzuki, T. Katayama, P. Bruno, S. Yuasa, and E. Tamura, Phys. Rev. Lett. **80**, 5200 (1998).
[43] Y.-L. He and G.-C. Wang, Phys. Rev. Lett. **70**, 2336 (1993).
[44] Q. Jiang, H.-N. Yang, and G.-C. Wang, Phys. Rev. B **52**, 14911 (1995).
[45] J.-S. Suen and J. L. Erskine, Phys. Rev. Lett. **78**, 3567 (1997).
[46] A. Berger, S. Knappmann, and H. P. Oepen, J. Appl. Phys. **75**, 5598 (1994).
[47] D. Guarisco, R. Burgermeister, C. Stamm, and F. Meier, Appl. Phys. Lett. **68**, 1729 (1996).
[48] P. Vavassori, V. Metlushko, R. M. Osgood III, M. Grimsditch, U. Welp, G. Crabtree, W. Fan, S. R. J. Brueck, B. Ilic, and P. J. Hesketh, Phys. Rev. B **59**, 6337 (1999).
[49] Y. Souche, V. Novosad, B. Pannetier, and O. Geoffroy, J. Magn. Magn. Mater. **177–181**, 1277 (1998).
[50] D. van Labeke, A. Vial, V. Novosad, Y. Souche, M. Schlenker, and A. D. Dos Santos, Opt. Commun. **124**, 519 (1996).
[51] M. Rührig, R. Schäfer, A. Hubert, R. Mosler, J. A. Wolf, S. Demokritov, and P. Grünberg, Phys. Status Solidi A **125**, 635 (1991).
[52] W.-H. Yeh, J. Carriere, and M. Mansuripur, Appl. Opt. **38**, 3749 (1999).
[53] L. H. Bennett, R. D. McMichael, L. J. Swartzendruber, S. Hua, D. S. Lashmore, A. J. Shapiro, V. S. Gornakov, L. M. Dedukh, and V. I. Nikitenko, Appl. Phys. Lett. **66**, 888 (1995).
[54] M. R. Pufall, A. Berger, and S. Schultz, J. Appl. Phys. **81**, 5689 (1997).
[55] J. B. Kortright, D. D. Awschalom, J. Stohr, S. D. Bader, Y. U. Idzerda, S. S. P. Parkin, I. K. Schuller, and H.-C. Siegmann, J. Magn. Magn. Mater. **207**, 7 (1999).
[56] J. F. Dillon, Jr., E. Y. Chen, N. Giordano, and W. P. Wolf, Phys. Rev. Lett. **33**, 98 (1974).
[57] V. V. Eremenko, N. F. Kharchenko, and L. I. Beliy, J. Appl. Phys. **50**, 7751 (1979).
[58] V. V. Eremenko and N. F. Kharchenko, J. Magn. Soc. Jpn. **11**, Supplement, No. S1, 27 (1987).
[59] J. Stöhr, A. Scholl, T. Regan, S. Anders, J. Lüning, M. R. Scheinfein, H. A. Padmore, and R. L. White, Phys. Rev. Lett. **83**, 1862 (1999).
[60] R. M. Osgood III, S. D. Bader, B. M. Clemens, R. L. White, and H. Matsuyama, J. Magn. Magn. Mater. **182**, 297 (1998).
[61] *Nonlinear Optics in Metals*, edited by K. H. Bennemann (Clarendon, Oxford, 1998).
[62] See, for example, T. Rasing, in Ref. 61.
[63] J. M. Florczak and E. D. Dahlberg, J. Appl. Phys. **67**, 7520 (1990); Phys. Rev. B **44**, 9338 (1991).
[64] A. Berger and M. R. Pufall, Appl. Phys. Lett. **71**, 965 (1997); J. Appl. Phys. **85**, 4583 (1999).
[65] M. R. Pufall, C. Platt, and A. Berger, J. Appl. Phys. **85**, 4818 (1999).
[66] W. A. McGahan and J. Woollam, Appl. Phys. Commun. **9**, 1 (1989).
[67] M. Mansuripur, J. Appl. Phys. **67**, 6466 (1990).
[68] S. Visnovsky, M. Nyvlt, V. Prosser, R. Lopusnik, R. Urban, J. Ferré, G. Pénissard, D. Renard, and R. Krishnan, Phys. Rev. B **52**, 1090 (1995).
[69] K. R. Heim and M. R. Scheinfein, J. Magn. Magn. Mater. **154**, 141 (1996).
[70] C.-Y. You and S.-C. Shin, J. Appl. Phys. **84**, 541 (1998).
[71] R. Atkinson, J. Magn. Magn. Mater. **95**, 61 (1991); **95**, 69 (1991).
[72] C.-Y. You, S.-C. Shin, and S.-Y. Kim, Phys. Rev. B **55**, 5953 (1997).
[73] M. Kim, A. J. Freeman, and R. Wu, Phys. Rev. B **59**, 9432 (1999).
[74] P. M. Oppeneer, T. Maurer, J. Sticht, and J. Kübler, Phys. Rev. B **45**, 10924 (1992).
[75] G. Y. Guo and H. Ebert, Phys. Rev. B **50**, 10377 (1994).
[76] T. Gasche, M. S. S. Brooks, and B. Johansson, Phys. Rev. B **53**, 296 (1996).
[77] V. N. Antonov, B. N. Harmon, A. Y. Perlov, and A. N. Yaresko, Phys. Rev. B **59**, 14561 (1999).
[78] V. N. Antonov, B. N. Harmon, A. N. Yaresko, and A. Y. Perlov, Phys. Rev. B **59**, 14571 (1999).
[79] Z. Q. Qiu, J. Pearson, and S. D. Bader, Phys. Rev. B **46**, 8195 (1992).
[80] E. R. Moog, S. D. Bader, and J. Zak, Appl. Phys. Lett. **56**, 2687 (1990).
[81] J. H. Weaver, in *CRC Handbook of Chemistry and Physics*, 69th ed., edited by R. C. Weast, M. J. Astle, and W. H. Beyer (CRC, Boca Raton, 1988), p. E-387ff.
[82] M. D. Mermin and H. Wagner, Phys. Rev. Lett. **17**, 1133 (1966).
[83] D. Pescia and V. L. Pokrovsky, Phys. Rev. Lett. **65**, 2599 (1990).
[84] D. P. Pappas, K.-P. Kämper, and H. Hopster, Phys. Rev. Lett. **45**, 8169 (1992).
[85] Z. Q. Qiu, J. Pearson, and S. D. Bader, Phys. Rev. Lett. **70**, 1006 (1993).
[86] D. P. Pappas, C. R. Brundle, and H. Hopster, Phys. Rev. B **45**, 8169 (1992).
[87] Y. Yafet and E. M. Gyorgy, Phys. Rev. B **38**, 9145 (1988).
[88] A. Kashuba and V. L. Pokrovsky, Phys. Rev. Lett. **70**, 3155 (1993); Phys. Rev. B **48**, 10335 (1993).
[89] R. Allenspach and A. Bischof, Phys. Rev. Lett. **69**, 3385 (1992).
[90] A. Berger and H. Hopster, Phys. Rev. Lett. **76**, 519 (1996).
[91] D. Wang, R. Wu, and A. J. Freeman, Phys. Rev. Lett. **70**, 869 (1993), and references therein.
[92] A. Berger, U. Linke, and H. P. Oepen, Phys. Rev. Lett. **68**, 839 (1992).
[93] W. Weber, C. H. Back, A. Bischof, Ch. Würsch, and R. Allenspach, Phys. Rev. Lett. **76**, 1940 (1996).
[94] J. Chen and J. Erskine, Phys. Rev. Lett. **68**, 1212 (1992).
[95] H. J. Choi, Z. Q. Qiu, J. Pearson, S. J. Jiang, D. Li, and S. D. Bader, Phys. Rev. B **57**, R12713 (1998).
[96] H. J. Choi, R. K. Kawakami, E. J. Escorcia-Aparicio, Z. Q. Qiu, J. Pearson, J. S. Jiang, Dongqi Li, and S. D. Bader, Phys. Rev. Lett. **82**, 1947 (1999).
[97] R. K. Kawakami, M. O. Bowen, H. J. Choi, E. J. Escorcia-Aparicio, and Z. Q. Qiu, Phys. Rev. B **58**, R5924 (1998).
[98] R. K. Kawakami, E. J. Escorcia-Aparicio, and Z. Q. Qiu, Phys. Rev. Lett. **77**, 2570 (1996).
[99] L. Néel, J. Phys. Radium **15**, 225 (1954).
[100] O. Rader, E. Vescovo, J. Redinger, S. Blügel, C. Carbone, W. Eberhardt, and W. Gudat, Phys. Rev. Lett. **72**, 2247 (1994).
[101] C. Liu and S. D. Bader, Phys. Rev. B **44**, 2205 (1991).